

Bubble Size Detection by Process Ancillaries

Lukas Hafner^{1,2,*}, Robin Bäßler¹, Steffen Schwarzer¹, Markus Kley¹, and Fadi Dohnal^{2,3}

DOI: 10.1002/cite.202100175

 This is an open access article under the terms of the Creative Commons Attribution-NonCommercial License, which permits use, distribution and reproduction in any medium, provided the original work is properly cited and is not used for commercial purposes.



Supporting Information
available online

The production of liquid-gas dispersions places high demands on the process technology, which requires knowledge of the bubble formation mechanisms, as well as the phase parameters of the media combinations used. To obtain the bubble sizes introduced to a flow not knowing the phase parameters, different process parameters are investigated. Their quality and applicability are evaluated. The results obtained make it possible to simplify long design processes of dispersion processes in manufacturing plants and to ensure the product quality of the products manufactured, by reducing waste.

Keywords: Bubble detection, Condition monitoring, Process appliances, Process technology

Received: September 23, 2021; *revised:* April 20, 2022; *accepted:* May 03, 2022

1 Introduction

The production of liquid-gas dispersions places high demands on process technology and can be found in industrial sectors such as the chemical industry, the plastics industry, the automotive industry and also the food industry [1–3]. Dispersion processes are used there to intersperse liquids with air, producing plastic foam, or metal foam for lightweight structures. In the food industry, products are foamed with blowing agents to improve mouthfeel and taste, for example. In the design of dispersion processes, the size and quantity of air bubbles introduced into the liquid are the target variables that decide the quality and stability of the end product. In order to be able to make a statement about the size and quantity of the introduced air bubbles, it is necessary either to know all phase and process variables, which is not feasible as shown later, or to go through elaborate high-speed video-based design processes [4, 5]. To perform a high-speed video-based design, it is necessary that the fluid into which the air is introduced is optically transparent. Unless the fluid is optically transparent, iterative design processes must be used. In addition to high-speed video-based design processes, X-ray images or ultrasonic images are also possible in some cases, but these provide much poorer resolutions and are therefore not applicable for most applications [3, 4, 6].

When performing high-speed video-based design processes, the air bubbles introduced into a fluid are measured optically. The size of the introduced air bubbles is measured as well as the frequency of the air bubble injection [1, 7]. These two quantities are combined in maps that are used to control the dispersion processes. Factors on which the sizes of the introduced air bubbles depend are geometric factors,

which cannot be changed easily, and process-related factors, some of which can be changed and some of which can vary unintentionally [1, 8, 9].

The geometrical factors that influence the size of the introduced air bubbles are the pipe diameter through which the liquid is conveyed, the type and number of air introduction points, the diameter of the air introduction hole but also the orientation of the air introduction hole to the direction of flow of the liquid [1, 8, 10].

The process-related factors are, e.g., the viscosity of the liquid used, the velocity of the liquid, the velocity of the air introduced into the liquid, the temperature of the air introduced, the surface tension between the liquid and the air, but also the prevailing pressures at the dispersion point [1, 10]. Process factors that can vary unintentionally include temperature, viscosity, or even pressure in the dispersion process [8]. The unintentional variation of the process factors arises, e.g., from the dispersion of the composition of the mixed phases. For example, a batch change of the

¹Lukas Hafner, Robin Bäßler, Prof. Dr.-Ing. Steffen Schwarzer, Prof. Dr.-Ing. Markus Kley
lukas.hafner@hs-aalen.de
Hochschule Aalen, Institut für Antriebstechnik, Beethovenstraße 1, 73430 Aalen, Germany.

²Lukas Hafner, a.o. Univ.-Prof. Dr. techn. Fadi Dohnal
UMIT – Private Universität für Gesundheitswissenschaften, Medizinische Informatik und Technik, Division for Mechatronics, Linker Inselweg 21, 9900 Lienz, Austria.

³a.o. Univ.-Prof. Dr. techn. Fadi Dohnal
FH Vorarlberg, CAMPUS V, Forschungszentrum Mikrotechnik, Hochschulstraße 1, 6850 Dornbirn, Austria.

materials used changes the viscosity ratio between the two mixed phases, which causes a change in the surface tension between the two materials.

With the help of high-speed video recordings, characteristic diagrams can only be created with considerable effort depending on batch variations, which quickly makes these processes unprofitable because of poor robustness. Furthermore, high-speed video-based design processes represent only a relatively short time range of the dispersion process, which may lead to a quite inaccurate design of a dispersion process that is continuous in nature. In order to enable a reliable design based on a longer time range without generating enormous amounts of data, the process parameters are investigated thoroughly in the present work. On the basis of the knowledge gained and the results generated, there are considerable advantages over a high-speed video-based design. For example, the sensor technology used can be established as a condition monitoring system through targeted use in the dispersion process, which prevents unwanted quality deviations in the manufactured products and thus enables a reliable statement to be made about the product quality. In addition, air injection points do not have to be manufactured transparently to enable a design of the dispersion processes. The tests carried out are performed with the media combination of oil and air. The data is compared by means of time-synchronized high-speed video recordings for verification.

2 State of the Art

According to the current state of the art, the air bubble size introduced into a flow can be measured using different measurement methods. These include ultrasonic imaging [4], X-ray imaging [3] and optical measurement methods in which air bubble flows are evaluated with high-speed camera images [2–4, 8, 11–16]. To apply much simpler and automatable measuring methods, the process ancillary variables occurring during the dispersion process are to be investigated with regard to their significance for the process stability and the quality of the signal. This means that no knowledge of the physical processes acting during the measurement is necessary.

2.1 Calculation of the Expected Process Ancillary Variables

2.1.1 Detection by Acoustic Process Ancillary Variables

One way to evaluate the air bubbles introduced into a liquid in terms of bubble size is to monitor the noise emission generated during air bubble dispersion. Studies have already investigated the eigenfrequency of air bubbles at different pressures and air volumes [17]. The eigenfrequency of oscil-

lation f_0 can be calculated by considering the density of the liquid ρ , into which air bubbles are introduced, the ambient pressure p , the adiabatic exponent γ and the air bubble radius r .

$$f_0 = \frac{1}{2\pi r} \sqrt{\frac{3\gamma p}{\rho}} \quad (1)$$

If it is assumed that the air bubble experiences an impulse when it is detached from the dispersing member, it follows that the dispersed air bubble is excited at a specific eigenfrequency of vibration: the resonance frequency of the lowest vibration mode. In addition to the impulse generated during air bubble detachment, interfering resonances can occur which can be perceived and thus have an influence on the quality of the measurement result. One of these spurious resonances is caused by the oscillation of the air bubble tube remaining at the air introduction point, represented by f_H in Fig. 1. When the air bubble detaches from the dispersion element, the opposite side of the detached and rising air bubble begins to oscillate [17]. Depending on the strength of the resulting impulse, this resonance overlaps the emitted resonance of the dispersed air bubble. The impulse at the air bubble tube remaining at the air insertion site causes the air insertion site itself to oscillate [1]. Particularly with regard to structure-borne sound detection by means of acceleration sensors, the resulting vibrations can influence the measurement result [18, 19]. The resonance frequency of the air injection point is represented by f_N in Fig. 1.

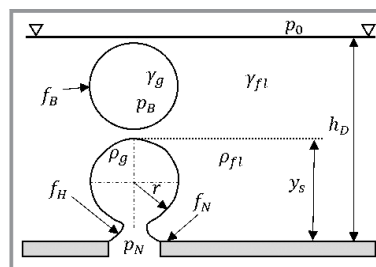


Figure 1. Representation of different influencing variables on the natural frequency of oscillation of the dispersed air bubbles with different resonance bodies; bubble frequency f_B , frequency of the bubblehose f_H , frequency of the nozzle f_N on basis of [3].

Different analysis methods are used to detect periodically recurring acoustic and vibration pulses. One common analysis method used to detect pulses is the envelope analysis. Envelope analysis is used primarily in signal analysis for fault and damage detection in roller bearings and other rotating machine elements. Here, non-stationary signals can be analyzed for recurring and periodic pulses, such as bearing damage [20–23]. To analyze such periodic pulses, it is necessary to divide the measurement signal into the instantaneous frequencies. A definition of a characteristic air bubble release frequency can thus be performed based

on the detection of the periodically recurring instantaneous frequency of a characteristic pulse.

Taking into account the set air volume flow \dot{V}_g and the period time Δt of an air bubble release process, the introduced air bubble volume V_B can be determined as follows.

$$V_B = \Delta t \dot{V}_g \quad (2)$$

By this method, in contrast to an optical measurement of the introduced air bubble volume, no approximation to an ideal geometric shape is necessary. This enables a much more accurate measurement result with a much lower measurement effort, which does not favor parallax errors, curvature effects or other negative characteristics of an optical measurement principle [5, 17, 24].

Another analysis method to be able to detect periodically recurring pulses is the examination of the time signal by a moving average and a limit value, which is evaluated as a minimum deviation criterion and thus as a pulse signal. This method can be used especially for non-stationary, but periodic, continuous and steady time signals. Depending on how large the gradient of the time signal is in relation to the expected expression of the event, the width of the time range to be averaged must be increased or decreased here. By a widening of the time range, over which a moving average is to be formed, it is compellingly necessary to consider that the expression of the expected impulse is reduced just like the expression of the time course between the impulses.

2.1.2 Detection by the Pressure in the Nozzle

There are already studies in which the pressure curves during the detachment of air bubbles in liquid media are calculated as a function of their surface tension σ , pressure p_0 , fluid density ρ_{Fl} and gas density ρ_g . The pressure curves to be expected can be derived from hydrostatic conditions, see Fig. 1 for more details [1].

$$p_N = \frac{2\sigma}{r} + p_0 + \rho_{Fl}gh_D - g(\rho_{Fl} - \rho_g)y_s \quad (3)$$

If we look at the pressure curve during the formation of the air bubbles, we can classify different areas of air bubble formation, see Fig. 2 based on Durst and Beer [1].

The first section (A) that can be seen in the characteristic pressure curve of an air bubble formation is the dome formation. In this region, the air bubble begins to form a volume above the nozzle. The second section (B) of air bubble formation is bubble bulging. As the air bubble gains height, due to the surface tension forces acting during air bubble formation, the bubble begins to constrict at its inflow. This is where the third section (C) of bubble formation begins: bubble constriction. This section ends with the loss of contact between the introduced air bubble and the nozzle. The air bubble rises due to the acting buoyancy force. Provided that the volume flow of the air supply is not interrupted, the

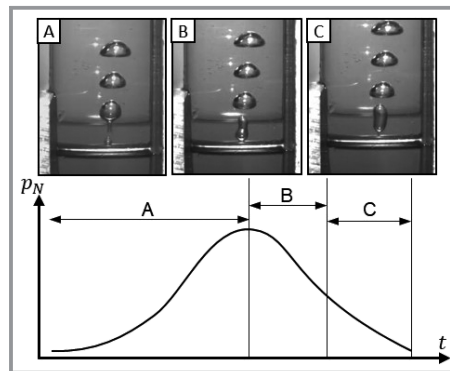


Figure 2. Different bubble formation stages based on [3].

air bubble formation process starts again at the area of dome formation (A). The pressure curve in the nozzle orifice, the bubble formation frequency or the size of the introduced air bubbles depends on the defined process parameters.

In air bubble formation, a distinction is made between two different bubble formation mechanisms: bubble gassing and jet gassing [25]. Bubble gassing is characterized by periodic detachment of individual bubbles from the air injection point, which retain their diameter during further ascent. In the case of the jet gassing bubble formation mechanism, air bubbles are formed which, in their further ascent, either break up into several smaller bubbles or merge to form larger bubbles. In the experiments presented here, only air bubbles formed by the bubble formation mechanism of the bubble gassing are considered. This avoids disturbance variables that negatively influence the measurement result and the information content of the results. The tests carried out are described in the following for signal 1 and signal 2.

Taking into account the duration of an air bubble formation cycle Δt and the volume flow rate filling the air bubble \dot{V}_g the diameter d_B of an introduced air bubble can be calculated.

$$d_B = 2\sqrt[3]{\frac{3\Delta t \dot{V}_g}{4\pi}} \quad (4)$$

Another way of obtaining information about process stability or the air bubble diameters introduced, taking into account the pressure curves during air dispersion, is to analyze the periodicity of the resulting pressure curves. For this purpose, the measured time signals are examined for recurring characteristic signals by means of frequency analyses.

2.2 Delimitation to the State of the Art

According to the current state of the art, the air bubble sizes introduced into a liquid flow can be measured by different

optical methods. Also, different process ancillary variables such as pressure and acoustic phenomena can be measured on dispersions. However, the process ancillary variables have not yet been used for condition monitoring to ensure product quality and to detect quality deviations. The work aims to examine the ancillary process variables that arise during a dispersion process and their significance for evaluation in the detection of process deviations. The dispersed air bubble diameter and the detachment frequency are measured non-invasively. The physical phenomena of the system detected in the process are measured by a microphone, an acceleration sensor and a pressure sensor. In order to be able to verify the presented approaches for the detection of the dispersed air bubble sizes, tests are carried out on a test rig, which is described in the following section.

3 Test Rig

The test rig setup for the tests is sketched in Fig. 3. The test rig consists of an acrylic glass tube with an inner diameter of $d_t = 27$ mm glued into an aluminum base body. A constant oil flow is conveyed through the acrylic glass. A steel tube is inserted into the acrylic glass tube transversely to the direction of flow, which has a hole of $d_N = 0.4$ mm in the direction of flow. A controlled air volume flow is introduced through this hole. The dispersion pressure, which is used to measure the introduced air bubble volumes, can be measured directly at the dispersion nozzle. An acceleration sensor is bonded to the aluminum housing, which detects the induced pulses of air bubble detachment due to the excited vibration of the housing. A measuring microphone is attached at a distance of 20 mm from the dispersion point to measure the acoustic pulses during the air bubble detachment. To identify the process sections specifically and reliably according to Fig. 2, time-synchronous high-speed camera recordings are taken of the dispersion point. Based on these high-speed camera recordings, the bubble formation frequency and the diameter of the introduced air bubbles can be measured. These two quantities are important for the analysis of the measurement signals of the pressure sensor, the microphone and the acceleration sensor in order to investigate the hypotheses presented in Sect. 1.

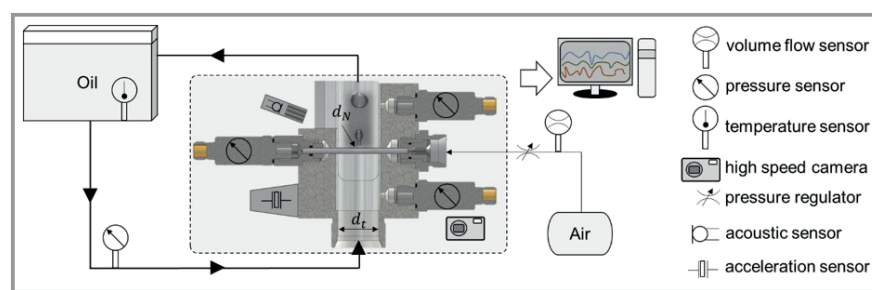


Figure 3. Schematic representation of the measurement setup.

4 Results

The test rig in Fig. 3 allows for reproducible results with a clear detection of the air bubble detachments. In the following the results obtained with the different sensor types used are presented and evaluated for their usability in industrial applications. All the tests carried out are recorded over a period of 30 s. The first 0.5 s of the measurement signal are recorded using a high-speed camera with a frame rate of 2.5 kHz.

4.1 Detection by Acoustic Process Ancillary Variables with Acceleration Sensors

During the conducted experiments, different measurement data evaluation methods are performed one after another to check the recorded sequences for the expected frequency of the expected signals. The approach of the evaluation of the acceleration sensor and the discussion of the corresponding results is presented in the following.

During one test cycle measured values are recorded over a period of 30 s at a sampling rate of 10 kHz with an acceleration sensor. The first 0.5 s are recorded with a high-speed camera at a frame rate of 2.5 kHz. These high-speed video recordings are used to verify the measurements and the generated results obtained. The measurement setup can be seen in Fig. 3. A block diagram of the sensors and data preprocessing used, as well as data postprocessing and the filters is visualized in Fig. 4.

As shown in Fig. 1, three different frequencies can be expected during the air bubble detachment process that are directly related to the air base detachment. Eq. (1) can be used to calculate the expected resonance frequency of the air bubble introduced into the oil over the air bubble radius. This equation is evaluated in Fig. 5. During the analysis of the high-speed videos, two different signals are recorded, optically measured and examined with respect to the bubble formation frequency. For signal 1, mean air bubble diameters of 1.95 mm to 2.03 mm are obtained. For signal 2, the mean air bubble diameters are measured between 2.0 mm and 2.12 mm. For the air bubble diameters produced during signal 1 and signal 2, air bubble eigenfrequencies between 480 Hz and 500 Hz are expected according to Eq. (1). A plot of the expected calculated air bubble eigenfrequency versus air bubble radius is shown in Fig. 5.

In order to enable a direct correlation between the generated high-speed camera recordings and the measurement data, only the time ranges between the measurement signals that are generated during the high-speed camera recordings are shown in the following graphs.

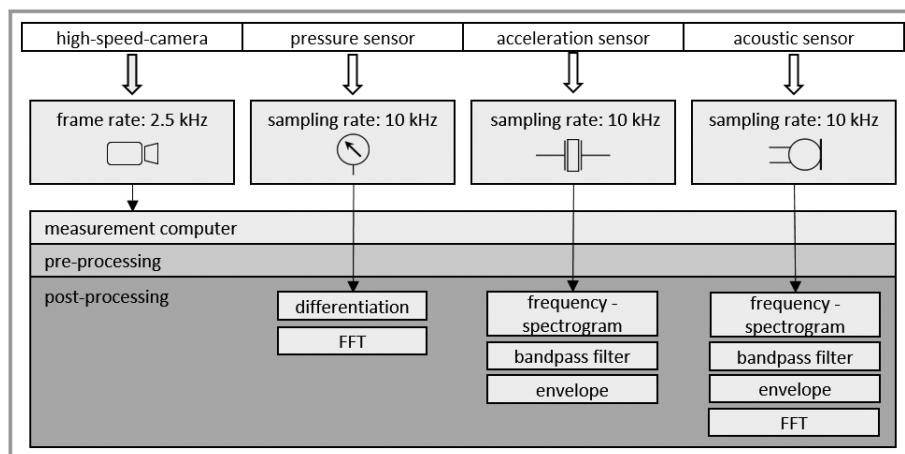


Figure 4. Block diagram of the experimental setup.

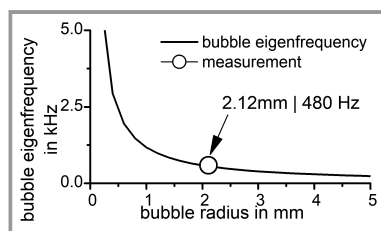


Figure 5. Eigenfrequency of the bubbles over the respective bubble radius.

Fig. 6 in line 1 shows an image section from the resulting high-speed images. The optically measured radius of the introduced air bubble is 2.03 mm. Line 2 shows the raw signal of the accelerometer for the time period between 0 s and 0.2 s. Since high-frequency and low-frequency interfering signals are superimposed on the actual measurement signal on the sampled measurement signal, frequency ranges are selected on the basis of performed time-dependent frequency spectrograms, which form the upper and lower cutoff frequencies for bandpass filters. The frequency spectrogram associated with the sampled measurement signal is shown in line 3 of Fig. 6. In the time-dependent frequency spectrogram, the intensities of the respective frequencies that make up the raw signal are plotted versus time. For the time range between 0 s and 0.2 s, several intensity maxima can be seen in periodic succession for signal 1. The intensity maxima are recognizable for the frequencies of 460 Hz, 2120 Hz, 3430 Hz and 4320 Hz. The strongest intensity maximum over the time range between 0 s and 0.2 s is recognizable for the frequency of 2120 Hz. In order to detect only the relevant frequencies in signal 1, a bandpass filter with a lower and upper cutoff frequency is specified. The frequency range of the bandpass filter defined for signal 1 is chosen between 1800 Hz and 2700 Hz. In signal 2, periodic intensity maxima can be detected for frequencies 680 Hz, 2190 Hz and 3340 Hz. The frequency range width for the bandpass filter defined for signal 2 is set for the frequency range between 1300 Hz and 3750 Hz.

The filter ranges for signal 1 and signal 2 are plotted in column 1 and column 2 with dashed lines in the time-dependent frequency spectrogram in line 3. The measured raw signal is filtered with a bandpass filter with Chebyshev characteristic of second order between the frequency range of 1800 Hz and 2700 Hz. Due to the weaker signal 2, a filter range between 1300 Hz and 3750 Hz is specified, filtering analogously to the filter function of signal 1 with a Chebyshev characteristic. The filtered time signals are shown in column 4 of Fig. 6. Based on the signal, pulses

with a periodic characteristic can be detected. To represent the periodic pulses more clearly, envelopes are used. The diagram of the maximum acceleration values of the time signal is created by adding the upper and lower envelope curves by amounts.

In Fig. 6, the time points of the maxima of the upper and lower envelope curve summed up by amounts are drawn with black and white circles in line 5. The measuring points with black background represent the snapshot from line 1. By determining the time interval between two maxima, the introduced air bubble diameters can be determined. The air bubble diameters in signal 1 calculated from the time interval match the optical evaluation of the air bubble diameters with a deviation of 0.09 mm on average. In signal 2, analogous to signal 1, the diameters of the introduced air bubbles can be calculated by the time interval between the occurring maxima. Here, the average deviations over the time period between 0 s and 0.2 s are 0.10 mm.

To depict the exact process of periodic air bubble detachment on the basis of the measurement signal, an entire air bubble detachment process with the associated image sequences from the high-speed camera recording is shown in Fig. 7. The measurement signal is signal 1 postprocessed according to Fig. 6 for the time range between 0.018 s and 0.053 s. The air bubble release process starts at point C and ends at point I. Between the start and the end of the air bubble detachment process there are three local maxima and two local minima. According to Durst and Beer [1], the bubble formation process can be divided into three regions, dome formation, bubble bulging, and bubble constriction, all of which can be demonstrated by the plotted points. Between point C and point D is the area of dome formation. This is where the strongest vibrations occur, which are very well detected by the accelerometer. Between point D and point F is the area of bubble bulging. Fewer vibrations occur in this area. Between point F and point I the bubble is cut off. At the end of point I, the introduced air bubble separates from the air introduction point and the air bubble

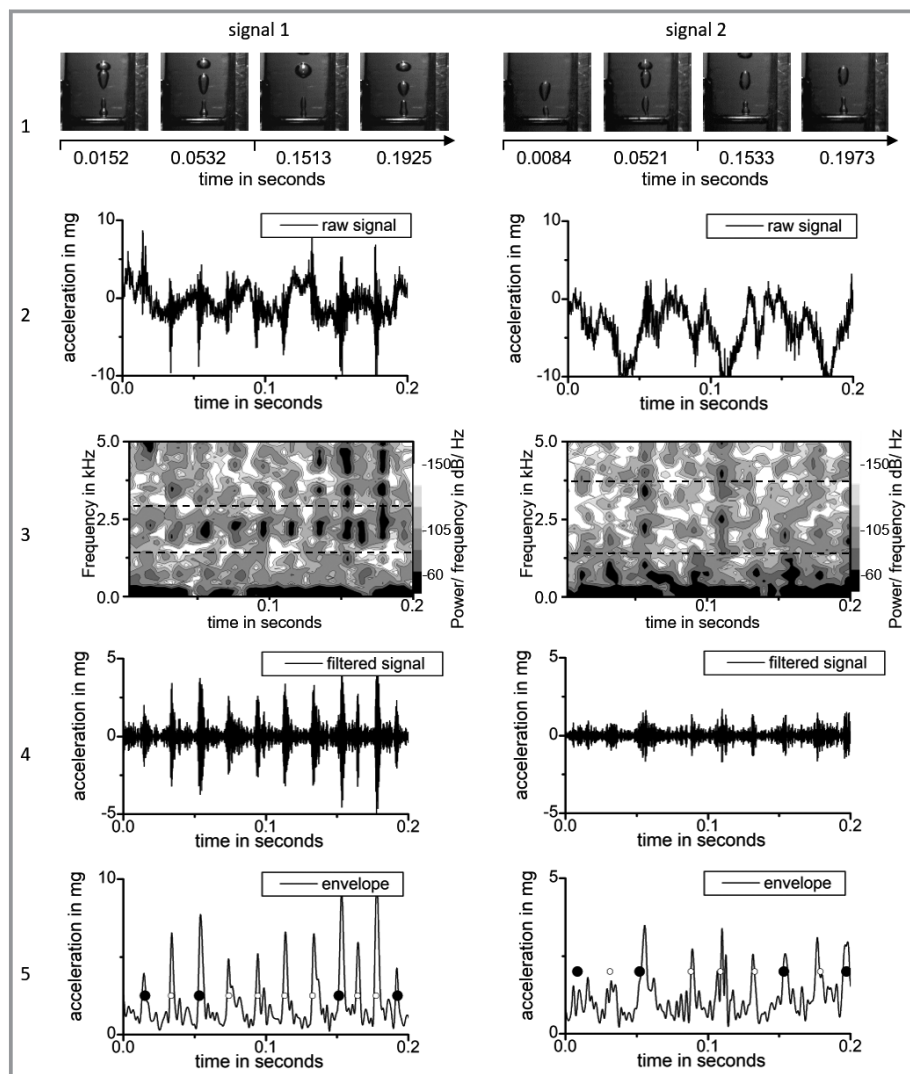


Figure 6. Signal processing of the measuring signals by the accelerometer sensor.

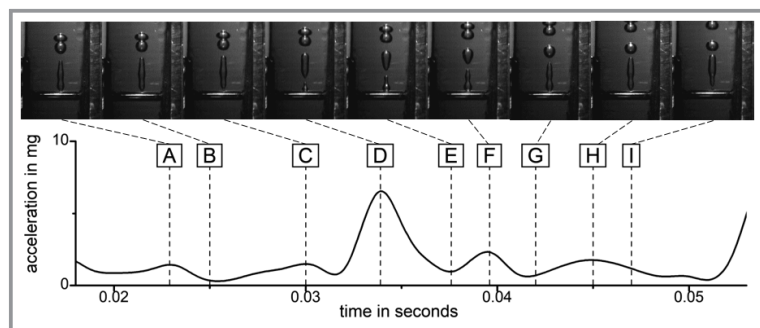


Figure 7. Accurate analysis of the air bubble release process using the signal 1 from Fig. 6, line 5.

formation process is complete. Point A and point B correspond to points H and I of a previous air bubble release process.

The magnitude of the maxima of the recorded acceleration values depends on the magnitude of the change in shape of the air bubble directly at the air introduction point. In the area of the dome formation, the air bubble has the largest surface contact area change to the air introduction point, seen over time. The forming forces during the formation of the air bubble cause vibrations which can be detected by the acceleration sensor. The magnitude of the acceleration values depends on the air bubble formation oscillation, the natural oscillation frequency and the oscillation capability of the air introduction point and the acting surface tension forces between the dispersed media.

4.2 Detection by Acoustic Process Ancillary Variables with Acoustic Sensors

In addition to the structure-borne sound recordings, the airborne sound is also recorded by a microphone during the tests. The microphone recordings are evaluated in the same way as the structure-borne sound recordings. The generated results are shown in Fig. 8.

The signals from the previous evaluation are recorded synchronously in time with the results shown here. Line 1 shows the recorded microphone signal of signal 1 and signal 2. To analyze periodic frequency maxima of the signal, a time-dependent frequency spectrogram can be created, as shown in line 2. For signal 1, periodic intensity maxima can be detected for the frequency range between 700 Hz and 2600 Hz. To evaluate the strength of the periodicity, the raw signal is filtered using a bandpass filter with Chebyshev characteristics between the lower cutoff frequency of 700 Hz and the upper cutoff frequency of 2600 Hz. By summing up the upper and lower envelope of the time signal by amounts, the time signal in line 3 is obtained.

Since no strong periodicity can be detected in this signal, an fast Fourier transform (FFT) analysis is used to examine the resulting signal for emerging intensity maxima. The

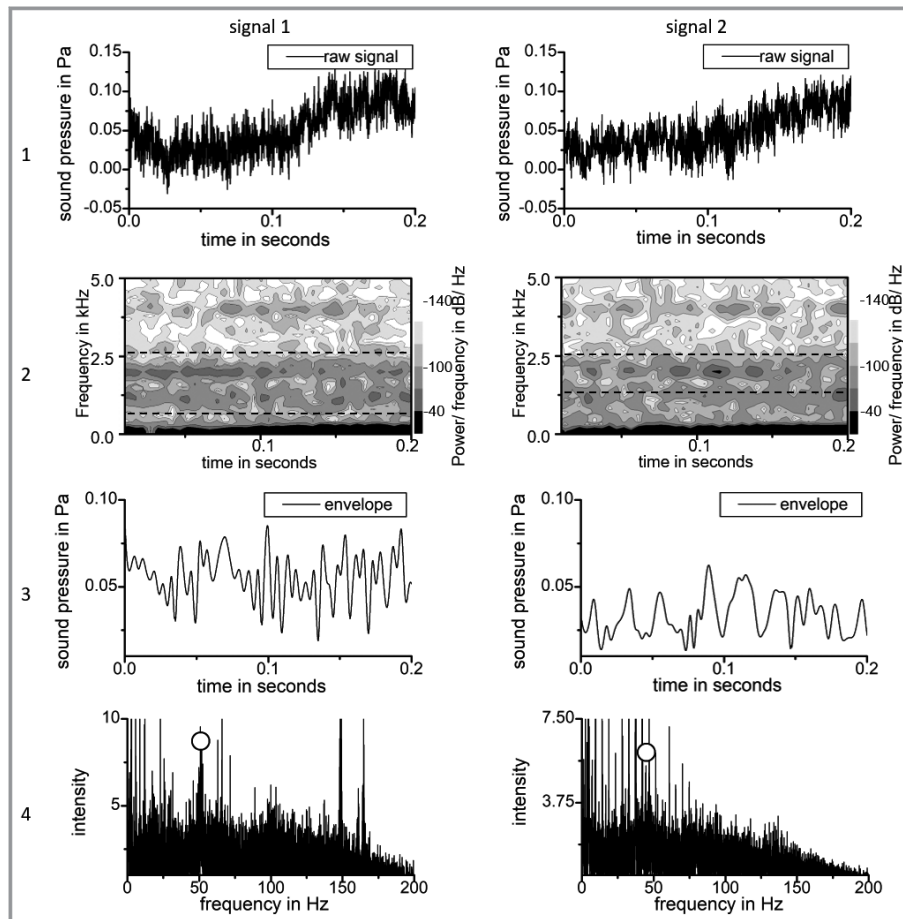


Figure 8. Signal processing of the measuring signals by the microphone sensor.

graph of the FFT analysis is shown in line 4. A strong pronounced maximum for the frequency of 51 Hz can be seen. By analyzing the high-speed video recordings taken during the tests, an average airbase detachment frequency between 51 Hz and 53 Hz is found. The air bubble detachment frequency measured by high-speed video recording analysis is drawn by a circle in the graph of the FFT analysis.

Signal 2 is evaluated in the same way as signal 1. The evaluation steps for this is shown in Fig. 8 in column 2. Line 1 again shows the measured raw signal. In the time-dependent frequency spectrogram (line 2), an intensity periodicity is detected for the frequency range between 1300 Hz and 2550 Hz. In this range, the same filter from signal 1 is applied for cutoff frequencies matched to it. The time signal of the upper and lower envelope of the filtered measurement signal is shown in line 3. By means of an FFT analysis, a frequency maximum can be determined for the frequency of 45 Hz. Based on the evaluation of the resulting high-speed camera recordings, an average air bubble release frequency of 43 Hz to 46 Hz can be determined for this time range.

4.3 Detection by the Pressure in the Nozzle

During the tests carried out, the pressure curves at the air injection point are recorded by pressure sensors with a sampling rate of 10 kHz. The pressure curves are recorded time-synchronously in the same way as for the acceleration sensors and the microphone recordings. The high-speed camera recordings also serve as a reference here.

Fig. 9 in line 1 shows the entire pressure curve over 30 s of a measurement. As can be seen, there is a pressure drop approximately each 2.5 s in the course of signal 1. This pressure drop is due to the volume flow control valve, which introduces a strong disturbance variable into the pressure signal due to the spring-biased throttling. In order to obtain a continuous signal for the evaluation, the pressure change per time step is calculated from the sampled measurement signal Fig. 9 line 1 in Fig. 9 line 2. When analyzing the high-speed camera recordings, the air bubble formation frequency is calculated. This lies between 51 Hz and 53 Hz for signal 1 and is drawn with a circle in line 3 in Fig. 9. To detect the bubble formation frequency on the basis of the pressure signal, frequency spectrograms are carried out using FFT analysis over a window width of 1 s. Due to the low frequency to be detected, only the frequency range between 0 Hz and 300 Hz is considered. The plot before three frequency spectrograms is shown in line 3 of Fig. 9. The air bubble formation frequency from 51 Hz to 53 Hz can be detected by FFT analyses over the entire signal 1.

The procedure for signal 2 is the same as for signal 1. Here, the bubble formation frequency is 43 Hz to 46 Hz according to the evaluation of the high-speed camera recordings. The interference signals of the volume flow controller occur much more frequently here. The range of the air bubble formation frequency verified by means of high-speed camera recordings is marked with a circle in line 3 of both diagrams.

Taking into account the results obtained by means of frequency spectral analysis, the volume of air introduced per air bubble and thus the diameter of the air bubbles introduced into the oil can be calculated. For signal 1, this results in a diameter of 3.97 mm according to Eq. (4). For signal 2, the

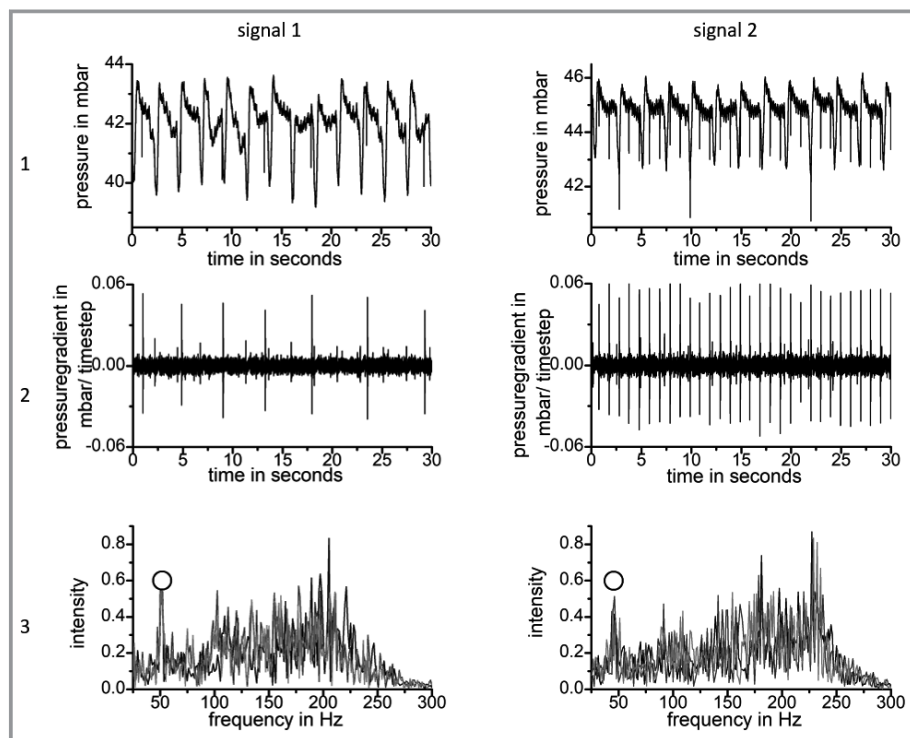


Figure 9. Signal processing of the measuring signals by the pressure sensor.

calculated diameter of the introduced air bubbles is 4.14 mm. The calculated values of the introduced air bubble diameters lie in the optically measured range. For signal 1, the optically measured air bubble diameters are between 3.90 mm and 4.06 mm. For signal 2, air bubble diameters between 4.00 mm and 4.24 mm are obtained. With renewed high-speed camera recordings with evaluation of the measurement data, the introduced bubble formation frequencies as well as the diameters of the introduced air bubbles can be reproduced.

5 Summary and Outlook

The tests carried out show that all three sensors used are suitable for measuring the air bubbles introduced into liquids. However, the quality of the generated results differs with respect to the accuracy of the measurement. Depending on the sensor used, it is possible to measure each individual air bubble or to calculate an averaged air bubble diameter over a time interval. Different evaluation steps are necessary to extract the results.

By evaluating the generated measurement data from the accelerometer, it is possible to calculate each individual air bubble introduced into the liquid. The generated results are reproducible and are verified by high-speed video recordings. The deviation between the optically evaluated results and the results extracted by means of accelerometer is at most 0.1 mm. Three evaluation steps are applied to be able to generate the result.

With the pressure sensor used, it is possible to calculate a moving average of the air bubble diameters introduced into the liquid. During the evaluation, the time range over which the mean air bubble diameters are calculated is reduced to one second. The air bubble diameters calculated in this process are within the tolerance range of the results measured by optical method. Two evaluation steps are required to extract the results. It is assumed that even more accurate results can be generated with further evaluation steps.

Using a microphone, it is possible to calculate the mean air bubble diameter introduced into the liquid over a time range of 10 s. The time range used is reduced by iterative loops. This measurement method is more susceptible to measurement errors due to the noise that can be generated in production equip-

ment or production lines. In further investigations, it must be considered to what extent acoustic shielding can simplify the evaluation in order to reduce the time range over which the mean air bubble diameter is measured.

In order to make a statement as to which sensor is best suited for the respective application, it is necessary on the one hand to know how accurate the desired result must be, but also which environmental factors can influence the measurement result. For an adaptation of these measuring principles in a production plant or manufacturing facility, the sensors used must be tested for their robustness and accuracy for the respective application.

Supporting Information

Supporting Information for this article can be found under DOI: <https://doi.org/10.1002/cite.202100175> (high-speed videos of the air bubble formation process from signal 1 and signal 2 in Fig. 6–9).

The authors acknowledge for the project Smart Bubble System, the technical support by testtec Prüfstands- und Bauteilerprobungs GmbH in Austria and the financial support within European program IraSME (ZIM: project number ZF4113820, FFG project number 877671). Open access funding enabled and organized by Projekt DEAL.

Symbols used

d_B	[m]	bubble diameter
d_T	[m]	tube diameter
d_N	[m]	nozzle diameter
f_B	[Hz]	bubble frequency
f_H	[Hz]	bubble hose frequency
f_N	[Hz]	frequency of the nozzle
p_B	[bar]	pressure of the bubble
p_N	[bar]	pressure in the nozzle
p_0	[Pa]	surrounding pressure
Δt	[s]	time period
\dot{V}_g	[m ³ s ⁻¹]	volume flow of gas
V_B	[m ³]	bubble volume

Greek letters

γ_{fl}	[-]	adiabatenexponent of the fluid
γ_g	[-]	adiabatenexponent of gas
ρ_g	[kg m ⁻³]	density of gas
ρ_{fl}	[kg m ⁻³]	density of fluid

References

- [1] F. Durst, H. Beer, *Chem. Ing. Tech.* **1969**, *18*, 1000–1006.
- [2] D. D. McClure, C. Wang, J. M. Kavanagh, D. F. Fletcher, G. W. Barton, *Chem. Eng. Res. Des.* **2016**, *106*, 205–213. DOI: <https://doi.org/10.1016/j.cherd.2015.12.027>
- [3] W. B. Hussein, S. A. Essmat, N. Yoma, *Int. J. Interact. Mob. Technol.* **2017**, *11* (2), 128–138. DOI: <https://doi.org/10.3991/ijim.v11i2.6590>
- [4] D. Bröder, *Anwendung optischer Messtechniken zur Untersuchung disperser Gas-Flüssigkeits-Strömungen*, Dissertation, ULB Sachsen-Anhalt **2003**.
- [5] M. Lichti, X. Cheng, H. Stephani, H. Bart, *Chem. Eng. Technol.* **2019**, *42* (2), 506–511. DOI: <https://doi.org/10.1002/ceat.201800340>
- [6] W. Hussein, M. S. Khan, J. Zamorano, F. Espic, N. B. Yoma, *Meas. Sci. Technol.* **2014**, *25* (12), 125302. DOI: <https://doi.org/10.1088/0957-0233/25/12/125302>
- [7] V. B. Fainerman, R. Miller, *Adv. Colloid Interface Sci.* **2004**, *108–109*, 287–301. DOI: <https://doi.org/10.1016/j.cis.2003.10.010>
- [8] P. Rollbusch, M. Bothe, M. Becker, M. Ludwig, M. Grünwald, M. Schlüter, R. Franke, *Chem. Eng. Sci.* **2015**, *126*, 660–678. DOI: <https://doi.org/10.1016/j.ces.2014.11.061>
- [9] L. Hafner, S. Schwarzer, F. Dohnal, *Chem. Ing. Tech.* **2021**, *93* (10), 1629–1635. DOI: <https://doi.org/10.1002/cite.202100023>
- [10] K. Terasaka, H. Tsuge, H. Matsue, *Can. J. Chem. Eng.* **1999**, *77*, 485–464.
- [11] D. P. Koller, P. M. Shankar, *Ultrasonics* **1994**, *32*, 229–233.
- [12] N. Q. Lu, A. Prosperetti, S. W. Yoon, *IEEE J. Oceanic Eng.* **1990**, *15* (4), 275–281. DOI: <https://doi.org/10.1109/48.103521>
- [13] R. Prakash, S. K. Majumder, A. Singh, *Ind. Eng. Chem. Res.* **2019**, *58* (8), 3499–3522. DOI: <https://doi.org/10.1021/acs.iecr.8b05625>
- [14] T. Alhashan, M. Elforjani, A. Addali, J. Teixeira, *Int. J. Eng. Res. Sci.* **2016**, *2*, 66–72.
- [15] H. Voit, R. Zeppenfeld, A. Mersmann, *Chem. Eng. Technol.* **1987**, *10*, 99–103.
- [16] N. B. Yoma, W. B. Hussein, M. S. Khan, F. S. Espic, J. A. Zamorano Navarro, *US 2017/0356882 A1*, **2017**.
- [17] P. Steinhauser, *Berg- Huettenmaenn. Monatsh.* **2020**, *165* (6), 260–264. DOI: <https://doi.org/10.1007/s00501-020-00976-1>
- [18] M. Bauer, F. Wagner, M. Kley, *TM, Tech. Mess.* **2021**, *88*, 674–685. DOI: <https://doi.org/10.1515/teme-2021-0045>
- [19] M. Frehner, H. Steeb, S. M. Schmalholz, in *Wave Propagation in Materials for Modern Applications* (Ed: A. Petrin), InTechOpen, London **2010**, 455–476. DOI: <https://doi.org/10.5772/6866>
- [20] Z. Feng, D. Zhang, M. J. Zuo, *IEEE Access* **2017**, *5*, 24301–24331. DOI: <https://doi.org/10.1109/ACCESS.2017.2766232>
- [21] R. Bäßler, M. Bauer, M. Kley, in *Beiträge zum 4. Aalener Kolloquium antriebstechnische Anwendungen*, Shaker Verlag, Düren **2020**, 112–117.
- [22] M. Bauer, R. Bäßler, M. Kley, in *Stuttgarter Symposium für Produktentwicklung SSP 2019 Stuttgart, 16. Mai 2019, Wissenschaftliche Konferenz*, Fraunhofer-Institut für Arbeitswirtschaft und Organisation, Stuttgart **2019**, 73–82. DOI: <https://doi.org/10.18419/opus-10394>
- [23] R. Bäßler, T. Bäßler, M. Kley, *TM, Tech. Mess.* **2022**, *89* (5), 352–362. DOI: <https://doi.org/10.1515/teme-2021-0143>
- [24] G. O. Berim, E. Ruckenstein, *Adv. Colloid Interface Sci.* **2016**, *231*, 15–22. DOI: <https://doi.org/10.1016/j.cis.2016.02.004>
- [25] A. Bals, *Chem. Ing. Tech.* **2002**, *74*, 337–344.